

Quantum vortex reconnections

S. Zuccher,¹ M. Caliarì,¹ A. W. Baggaley,^{2,3} and C. F. Barenghi³

¹*Dipartimento di Informatica, Facoltà di Scienze, Università di Verona, Ca' Vignal 2, Strada Le Grazie 15, 37134 Verona, Italy*

²*School of Mathematics and Statistics, University of Glasgow, Glasgow, G12 8QW, United Kingdom*

³*Joint Quantum Centre (JQC) Durham-Newcastle, and School of Mathematics and Statistics, Newcastle University, Newcastle upon Tyne, NE1 7RU, United Kingdom*

(Dated: 21 November 2012)

We study reconnections of quantum vortices by numerically solving the governing Gross-Pitaevskii equation. We find that the minimum distance between vortices scales differently with time before and after the vortex reconnection. We also compute vortex reconnections using the Biot-Savart law for vortex filaments of infinitesimal thickness, and find that, in this model, reconnection are time-symmetric. We argue that the likely cause of the difference between the Gross-Pitaevskii model and the Biot-Savart model is the intense rarefaction wave which is radiated away from a Gross-Pitaevskii reconnection. Finally we compare our results to experimental observations in superfluid helium, and discuss the different length scales probed by the two models and by experiments.

PACS numbers:

47.32.C- (vortex dynamics)

67.30.he (vortices in superfluid helium)

03.75.Lm (vortices in Bose Einstein condensates)

I. INTRODUCTION

The importance of vortex reconnections in turbulence¹ cannot be understated. Reconnections randomize the velocity field, play a role in the energy cascade, contribute to the fine-scale mixing, enhancing diffusion²⁻⁴, and are the dominant mechanism of jet noise generation. If the axes of tubular vortex structures are interpreted as the skeleton of turbulence, then the knottedness of the axes characterizes the turbulence's topology, and vortex reconnections are the critical events which change this topology⁵. This idealized picture becomes physical reality if one moves from ordinary viscous fluids to quantum fluids⁶ such as superfluid liquid helium (³He-B and ⁴He) and atomic Bose-Einstein condensates. In these superfluid systems, quantum mechanics constrains any rotational motion to vortex lines around which the circulation is fixed by the condition

$$\oint_C \mathbf{u} \cdot d\mathbf{r} = \frac{h}{m} = \kappa, \quad (1)$$

where \mathbf{u} is the velocity, C is a closed integration path around the vortex axis, h is Planck's constant, m is the mass of the relevant boson (a helium atom in the case of ⁴He, a Cooper pair in the case of ³He-B), and κ is the quantum of circulation. Another constraint of quantum mechanics is the small vortex core, which has fixed radius (10^{-8} cm in ⁴He, 10^{-6} cm in ³He-B) and is orders of magnitude smaller than the average distance between vortices in typical experiments; because of these constraints, no intensification or diminution of vorticity through stretching of the vortex core is possible in quantum fluids.

Vortex reconnections of individual quantum vortex lines are discrete, dramatic events, which have been recently visualized in the laboratory⁷. They are the key to understanding quantum turbulence⁸, a disordered state of vortex lines which is easily created by stirring liquid helium and atomic condensates. Compared to quantum reconnections, viscous reconnections in ordinary (classical) fluids are not complete events: classical vorticity is continuous, not discrete, and parts of the initial vortical tubes can be left behind as vortex threads, which then undergo successive reconnections (the cascade and mixing scenarios), as newly formed vortex bridges recoil from each other by self-advection⁹. Another important difference is that classical reconnections are dissipative events: viscous forces turn part of the fluid's energy into heat, whereas in a superfluid the viscosity is zero, and the fluid's total energy is conserved.

It can be argued that, because of the utter simplicity of quantum vortices (zero viscosity, fixed circulation, small core size), quantum vortex reconnections are not only important phenomena of low temperature physics and of atomic physics, but are also relevant to our general understanding of fluid phenomena as toy models of Euler dynamics.

Although a rather large number of studies addressed the viscous reconnection problem, both the underlying mechanism and various scaling relationships have remained elusive¹. The first analytical work on classical vortex reconnections goes back to Crow¹⁰, who studied the instability of a pair of counter-rotating vortex tubes shed from the wing tips of an airplane. However, the systematic study of vortex reconnections began with observations and laboratory experiments of the simplest and most fundamental interaction of two colliding vortex rings^{11–13}. With the rapid development of supercomputers, direct numerical study of vortex reconnection became possible. Ashurst & Meiron¹⁴ numerically solved the incompressible Navier-Stokes equations in the region of closest approach of two vortex rings by providing an initial condition generated using the Biot-Savart (BS) model¹⁵ of vortex filaments. At the same time, Pumir & Kerr¹⁶ performed numerical simulations of interacting vortex tubes. Many other studies followed (for a review of the extensive work up to 1994 see the review of Kida & Takaoka¹), but the literature on classical vortex reconnections seemed to fade after 1994^{17–21}. The recent work by Hussain & Duraisamy⁹ renewed the interest in the mechanics of viscous vortex reconnection. Their study focused on the direct, high resolution numerical simulation of the incompressible Navier-Stokes equations over a wide range of vortex Reynolds numbers, Re , for two perturbed anti-parallel vortex tubes. They found that the minimum distance δ between the vortex tube centroids scales as $\delta(t) \sim (t_0 - t)^{3/4}$ before the reconnection and as $\delta(t) \sim (t - t_0)^2$ after the reconnection, where t is time and t_0 is the instant of smallest separation between the vortex centroids.

The literature concerned with quantum reconnections is more limited. The possibility of reconnections was first raised by Feynman²² in his pioneering work on the applications of quantum mechanics to superfluid helium. Schwarz^{23,24} realized that vortex reconnections are necessary to account for quantum turbulence. He modelled quantum vortices as classical vortex filaments and proposed the Local Induction Approximation (LIA²⁵) as a practical alternative to the exact (but CPU-intensive) Biot-Savart law for the numerical study of superfluid vortex dynamics.

A few years later, Koplik & Levine²⁶ performed the first numerical simulation of quantum vortex reconnections by solving the Gross-Pitaevskii equation (GPE) which governs the motion of a Bose-Einstein condensate and is used as a model of superfluid helium. They found that if two vortices are nearly anti-parallel when the large-scale fluid motion brings them together, they reconnect, thus confirming the conjecture of Feynman and Schwarz.

Soon after, using the vortex filament model of Schwarz, de Waele & Aarts²⁷ numerically integrated the Biot-Savart equation for the ideal-fluid velocity field and claimed the existence of a universal route to reconnection for all kind of initial vortex-antivortex arrangements: their calculations showed that, when vortices approach each other, they always form the same pyramidal cusp. They measured the minimum distance between vortices, δ , during the approach to reconnection as a function of time t , and found that

$$\delta(t) \approx \sqrt{\frac{\kappa}{2\pi}(t_0 - t)}, \quad (2)$$

where t_0 is the time of reconnection. Equation (2) is consistent with the dimensional argument that, if the only relevant parameter in reconnection dynamics is the quantum of circulation, then

$$\delta(t) = A(\kappa|t_0 - t|)^\alpha, \quad (3)$$

where $\alpha = 0.5$ and A is a dimensionless constant of order unity.

Leadbeater *et al.*²⁸ used the GPE model to study reconnections of vortex rings launched against each other, and discovered that a sound wave (in the form of a short rarefaction pulse) is emitted at a reconnection event. The wave turns part of the initial kinetic energy of the vortices into acoustic energy which is radiated away. Acoustic energy is also created by vortex acceleration^{29,30}. The effects are clearly important to make sense of the observed decay of quantum turbulence at very low temperatures³¹.

Individual quantum vortex reconnections were first observed by Paoletti *et al.*⁷ by analyzing the trajectories of solid hydrogen tracers in superfluid ⁴He. They verified that the scaling (3) with $\alpha = 0.5$ holds before and after the reconnections, that is to say quantum reconnections are statistically time reversible, unlike classical reconnections⁹. They concluded that the expression

$$\delta(t) = A(\kappa|t_0 - t|)^{1/2}(1 + c|t_0 - t|), \quad (4)$$

is the best fit to their data, with wide distribution of values centred around $A \approx 1.1$ (larger than $A = (2\pi)^{-1/2} \approx 0.4$ found by de Waele & Aarts²⁷) and $c \approx 0$.

The universality of the route to reconnections was questioned by Tebbs *et al.*³² who performed a series of numerical simulations of quantum reconnections using the GPE. They reproduced the pyramidal shape of the vortex lines observed by de Waele & Aarts²⁷ for the initial configuration used by these authors, but did not observe the same shape for other configurations. They also confirmed the scaling (3), again in agreement with de Waele & Aarts²⁷, but did not measure the time evolution of δ after the reconnection.

Kursa *et al.*³³ employed LIA, Biot-Savart and GPE simulations, and showed that a single reconnection of two almost anti-parallel quantum vortices can lead to the creation of a cascade of vortex rings, provided that the angle between the vortices is sufficiently small.

Kerr³⁴, by means of numerical simulation of the GPE, investigated the reconnection between a pair of perturbed anti-parallel quantum vortices. He argued that kinetic energy is converted into interaction energy and eventually local kinetic energy depletion that is similar to energy decay in a classical fluid, even though the governing equations are Hamiltonian and energy conserving.

The present study aims at characterizing vortex reconnection in quantum fluids by performing direct numerical simulations of the three-dimensional GPE in different vortex configurations. Our goal is to extract the minimum distance δ between vortices as a function of time, both before and after the reconnection, compare results against classical reconnections, quantum reconnections computed with the Biot-Savart law, and experiments in superfluid helium.

The plan of the paper is the following. In section II we introduce the governing GPE, cast it in dimensionless form, and present the straight vortex solution. In section III we describe the initial condition of our numerical calculations in terms of the initial angle β between the vortex lines, and present computed vortex reconnections, paying attention to the minimum distance δ between vortices before and after the reconnection, and the sound wave which is generated. We also perform reconnections using the Biot-Savart model. In section IV we compare GPE reconnections and Biot-Savart reconnections with previous work and experiments, and draw the conclusions. The numerical method which we use to solve the GPE is described in the Appendix.

II. MODEL

The governing equation for a weakly-interacting Bose-Einstein condensate is the GPE³⁵

$$i\hbar \frac{\partial \psi}{\partial t} = -\frac{\hbar^2}{2m} \nabla^2 \psi + V_0 |\psi|^2 \psi - E_0 \psi, \quad (5)$$

where $\psi(\mathbf{x}, t)$ the macroscopic single-particle wave function for N bosons of mass m at position \mathbf{x} and time t , V_0 is the strength of the repulsive interaction between the bosons, E_0 is the chemical potential (the energy increase upon adding a boson), $\hbar = h/(2\pi)$, and the normalization condition is

$$\int |\psi|^2 d\mathbf{x} = N. \quad (6)$$

To study atomic condensates rather than liquid helium, a term of the form $V_{\text{trap}}\psi$, where V_{trap} is a suitable trapping potential (usually harmonic), is added to the right hand side of equation 5. Hereafter we shall not consider such term, but limit our work to homogeneous condensates. When applying the GPE to superfluid helium we must remember that helium is a liquid, not a weakly interacting gas, so the GPE model is more qualitative than quantitative. For example, the dispersion relation of small perturbations from the uniform solution $\psi_\infty = \sqrt{E_0/V_0}$ of equation 5 is

$$\omega^2 = \frac{\hbar^2 k^4}{4m^2} + \frac{E_0}{m} k^2, \quad (7)$$

where ω is the angular velocity, k is the wavenumber and $c = \sqrt{E_0/m}$ is the speed of sound. Note that for $k \ll 1$ we have $\omega \approx ck$ (phonons), and for $k \gg 1$ we have $\omega \approx \hbar k^2/(2m)$ (free particles), without the roton minimum which is characteristic of superfluid helium⁶. Another shortcoming of the GPE is the vortex core: more sophisticated models of the helium vortex core exist³⁶, but are not practical for the study of complex dynamics such as vortex reconnections.

By applying the transformation

$$\mathbf{x} \rightarrow \frac{\hbar}{\sqrt{2mE_0}} \mathbf{x}, \quad t \rightarrow \frac{\hbar}{2E_0} t, \quad \psi \rightarrow \sqrt{\frac{E_0}{V_0}} \psi, \quad (8)$$

where $\psi_\infty = \sqrt{E_0/V_0}$ is the uniform solution at rest in an infinite domain, we cast the GPE in the following dimensionless form

$$\frac{\partial\psi}{\partial t} = \frac{i}{2}\nabla^2\psi + \frac{i}{2}(1 - |\psi|^2)\psi. \quad (9)$$

The quantity $\zeta_0 = \hbar/\sqrt{2mE_0}$ is called the healing length or coherence length. It is the typical length scale over which the wave function bends, and therefore determines the vortex core radius (see next section) and the thickness of any superfluid boundary layer in the presence of a wall.

The numerical method to numerically solve the GPE is described in the Appendix. Figure 1 (left) shows that during the time evolution the Hamiltonian energy, defined by

$$E = \int dV \left(\frac{1}{2}|\nabla\psi|^2 + \frac{1}{4}(1 - |\psi|^2)^2 \right) \quad (10)$$

is sufficiently well conserved: the numerical error is less than one part in 10^7 . The fluid dynamics interpretation of the GPE arises from the Madelung transformation

$$\psi = \sqrt{\rho}e^{iS}, \quad (11)$$

which yields the following equations

$$\frac{\partial\rho}{\partial t} + \frac{\partial(\rho u_j)}{\partial x_j} = 0, \quad (12)$$

$$\rho \left(\frac{\partial u_i}{\partial t} + u_j \frac{\partial u_i}{\partial x_j} \right) = -\frac{\partial p}{\partial x_i} + \frac{\partial \tau_{ij}}{\partial x_j}, \quad i = 1, 2, 3 \quad (13)$$

(written in tensorial notation), where density and velocity are

$$\rho = |\psi|^2, \quad \mathbf{u} = \nabla S, \quad (14)$$

and

$$p = \frac{\rho^2}{4} \quad \text{and} \quad \tau_{ij} = \frac{1}{4}\rho \frac{\partial^2 \ln \rho}{\partial x_i \partial x_j}, \quad (15)$$

are the pressure and the so-called quantum stress. It is easy to verify that the quantum stress term at the right hand side of in equation (13) is negligible compared to the pressure term at length scales larger than unity (the coherence length). Since, as we shall see, the vortex core radius is of the order of the coherence length, we conclude that, at scales larger than the vortex core, the GPE, expressed by equations (12) and (13), reduces to the classical (compressible) Euler equations. Incompressible Euler dynamics is achieved in the further limit of small velocity (compared to the sound speed $c = \sqrt{E_0/m}$) at constant density (again, away from the vortex cores).

We seek a two-dimensional solution of equation (9) that represents a straight vortex centred at the origin. It is well-known that the classical two-dimensional Euler vortex of circulation Γ has azimuthal velocity $u_\theta = \Gamma/(2\pi r)$ where $r = \sqrt{x^2 + y^2}$ is the radius and $\theta = \arctan(y/x)$ is the azimuthal angle. The Cartesian components of the velocity are thus $u_x = -u_\theta \sin \theta = -\Gamma y/(2\pi r^2)$ and $u_y = u_\theta \cos \theta = \Gamma x/r^2$. Therefore $\mathbf{u} = (u_x, u_y) = (\Gamma/(2\pi))\nabla\theta$. This shows that the velocity field is solenoidal ($\nabla \cdot \mathbf{u} = 0$), that the quantum mechanical phase, S , is simply the azimuthal angle θ , and that the quantum of circulation, in our dimensionless units, is equal to 2π . In steady conditions, the continuity equation ensures that $\nabla \cdot (\rho\mathbf{u}) = 0$, hence $\mathbf{u} \cdot \nabla\rho = 0$, which means that $\nabla\rho \cdot \nabla\theta = 0$. The solution $\rho = \text{const}$ has infinite energy and must be rejected. The other possibility is that $\nabla\rho \perp \nabla\theta$. Since the cylindrical coordinates r and θ are perpendicular to each other, $\nabla\theta$ is parallel to r , hence $\nabla\rho$ is perpendicular to r . Therefore, for a steady two-dimensional and divergence-free velocity field, we must have $\rho = \rho(r)$. Seeking a solution which represents a vortex centred at the origin, we set $\psi = \sqrt{\rho}e^{iS} = f(r)e^{i\theta}$ where $f(r)$ is a function to be determined. By imposing that ψ is the steady solution of equation (9), we find that $f(r)$ satisfies the equation

$$f'' + \frac{f'}{r} + f \left(1 - f^2 - \frac{1}{r^2} \right) = 0 \quad (16)$$

with boundary conditions $f(0) = 0$, $f(\infty) = 1$. The equation can be integrated numerically, but, to make the computation of the initial condition faster, we look for a Padé approximation $R(r)$ to $f(r)$ of the form

$$R(r) = \frac{\sum_{j=0}^m p_j r^j}{1 + \sum_{k=1}^n q_k r^k} = \frac{p_0 + p_1 r + p_2 r^2 + \dots + p_m r^m}{1 + q_1 r + q_2 r^2 + \dots + q_n r^n}, \quad (17)$$

which agrees with $f(r)$ at the origin to the highest possible order, i.e. $f(0) = R(0)$, $f'(0) = R'(0)$, $f''(0) = R''(0)$, \dots , $f^{(m+n)}(0) = R^{(m+n)}(0)$. In our case $\rho \geq 0$, and the Padé approximation can be limited to⁴⁰

$$\rho(r) \approx \frac{r^2(c_1 + c_2 r^2)}{1 + c_3 r^2 + c_2 r^4}, \quad (18)$$

with

$$c_1 = \frac{11}{32}, \quad c_3 = \frac{5 - 32c_1}{48 - 192c_1}, \quad c_2 = c_1 \left(c_3 - \frac{1}{4} \right). \quad (19)$$

The quantum vortex core is thus a hole of radius of the order of a_0 around which the quantum mechanical phase changes by 2π . Figure 1 (right) compares the radial profile of the density near the vortex axis computed numerically and with the Padé approximation.

III. RESULTS

A. GPE initial condition

Our initial condition consists of two straight vortex lines \mathbf{v}_1 and \mathbf{v}_2 as in figure 2 (the arrow denotes the direction of the vorticity), which intersect the y -axis respectively at the points C_1 and C_2 . We call π_1 the y - z plane, π_2 the plane perpendicular to π_1 and passing through C_2 , and s the intersection between π_1 and π_2 . We call β the angle formed by the directions \mathbf{v}'_1 and \mathbf{v}_2 , where \mathbf{v}'_1 is the projection of \mathbf{v}_1 onto π_2 . In the case of two parallel vortices we have $\beta = 0$; in the case of two anti-parallel vortices we have $\beta = \pi$. Perpendicular intersections occur for $\beta = \pi/2$ and $\beta = -\pi/2$ (the latter is shown at the right of figure 2).

B. GPE reconnection of anti-parallel vortices

Our first numerical experiment is concerned with the reconnection of anti-parallel vortex lines (reconnecting angle $\beta = \pi$). The size of the computational box is $-30 \leq x, y, z \leq 30$. At time $t = 0$ the vortex lines are located at position $(x_0; y_0) = (10; \pm 3)$. In order to make sure that the reconnection occurs in the centre of the computational domain, we impose a slight initial perturbation to the vortex lines, of the form $A [\cos(2\pi(z_{\max} - z_{\min})/\lambda)]^6$. Figure (3) shows some snapshots of the time-evolution. It is apparent that the two vortices move as a pair in the x -direction. The slight initial curvature enhances the Crow instability and the vortices approach each other. The reconnection results in the formation of two U-shaped vortex lines, which bend and move apart from each other.

Figure (4) shows the minimum distance δ between reconnecting vortices as a function of time t . The algorithm to compute δ searches for vortex lines, starting from the boundaries, following the minimum of the density ρ . Once the vortex lines are retrieved, they are put in parametric form as curves in \mathbb{R}^3 , i.e. $\mathbf{r}(\xi) = (x(\xi), y(\xi), z(\xi))$, and δ is computed. Our main finding is that $\delta(t)$ behaves differently before and after the reconnection. In this respect, quantum vortex reconnections are therefore similar to viscous reconnections. Indeed figure (3) resembles very closely figure (3b) of Hussain & Duraisamy⁹.

C. GPE reconnection of vortices at different initial angles

We perform several other numerical calculations of vortex reconnections to check whether the time dependence of $\delta(t)$ depends on the angle β of the initial condition. Figure (5) shows the time evolution of two initially straight vortices set at the angle $\beta = 3\pi/4$. Again, we observe that the vortices first approach each other, then move away after the reconnection. A very similar behavior characterizes vortices initially set at $\beta = \pi/2$ (orthogonal reconnection), whose time-evolution is shown in figure (6).

Figure (7) summarizes the results obtained for different values of β . The minimum distance between the vortices, δ , is reported separately before and after reconnection as a function of $|t - t_0|$, where t_0 is the time at which the vortex reconnection takes place. Power laws (black solid lines) of the form

$$\delta = A|t - t_0|^\alpha, \quad (20)$$

(where δ and $t - t_0$ are dimensionless) are super-imposed to fit the numerical data; the fitting coefficients A and α are reported in table I. From Figure (7) and table (I) we conclude that GPE reconnections are not time-symmetric: the average values of α is $\alpha = 0.39$ before the reconnection and $\alpha = 0.68$ after the reconnection. If we average all values, before and after, we obtain $\alpha = 0.53$, which is in fair agreement with $\alpha = 0.5$ predicted by the scaling argument (3). Table (I) also shows that the average values of A are $A = 1.29$ before the reconnection and $A = 1.54$ after the reconnection. If we set $\alpha = 0.5$ and return to dimensional variables, we obtain $A = 1.29/\sqrt{2\pi} = 0.52$ and $1.54/\sqrt{2\pi} = 0.62$, which are about half of the value $A \approx 1.1$ found by Paoletti *et al.*⁷ in their experiment.

As a check, we repeat all numerical simulations for opposite angles (e.g. $\beta = \pm\pi/2$, $\beta = \pm\frac{3}{4}\pi$, etc.) obtaining the same temporal dependence of δ upon time t .

D. GPE reconnection wave

Our calculation confirms the finding of Leadbeater *et al.*²⁸, that a vortex reconnection creates a wave. First we consider the reconnection of anti-parallel vortices ($\beta = \pi/2$). By extracting the iso-surfaces at quite large level, as done in figure (8) for $\rho = 0.94$, one notices the formation of a mushroom-shaped pressure (density) rarefaction wave generated by the reconnection. The wave becomes shallower as it moves away from the vortices. The bottom plot of figure (8) shows the vortex lines together with the pressure wave obtained by replacing the vortex tubes from the isosurface at $\rho = 0.94$ with the isosurface at $\rho = 0.2$. The footprint of the wave is particularly visible in contours of ρ on the plane $y = 0$, as shown in figure (9).

The pressure wave is clearly visible for relatively small angles between vortices, $\beta < \pi/2$, whereas for larger angles it becomes difficult to clearly track it and visualize it. Figure (10) shows the time evolution of the mushroom-shaped pressure wave ejected after reconnection for $\beta = 7\pi/8$ (isosurfaces at $\rho = 0.94$).

E. GPE reconnections and vortex rings

As we have mentioned in Section I, secondary generation of vortex rings following a reconnection event was observed in the numerical simulations of Kursa *et al.*³³ and Kerr³⁴. Kursa *et al.* also studied how the emission of vortex rings depends on the initial angle between the vortices (almost antiparallel configurations favour the generation of vortex rings following the Crow instability). We do not investigate further the generation of vortex rings, since it was already studied in detail in cited works. We only remark that if we make our computational box longer in the z direction, vortex rings generation becomes visible, as shown in figure 11. As for the physical significance of this effect, we notice that, according to a recent study of Baggaley *et al.*⁴¹, the distribution of reconnecting angles β depends on the nature of the quantum turbulence. Quantum turbulence generated with grids or propellers seems classical in nature (for example the kinetic energy is distributed on the length scales according to the classical Kolmogorov $k^{-5/3}$ law where k is the wavenumber), and contains coherent bundles of vortices which induce reconnections at small angles β . On the contrary, quantum turbulence generated thermally (e.g. counterflow turbulence) is spatially more random, and reconnections tend to be antiparallel ($\beta \approx \pi$).

F. Biot-Savart reconnections

It is instructive to compare reconnections computed with the GPE with reconnections computed with the Biot-Savart law. The latter, which is widely used to study quantum turbulence, approximates vortex lines as space curves $\mathbf{s} = \mathbf{s}(\xi, t)$ of infinitesimal thickness which move according to

$$\frac{d\mathbf{s}}{dt} = -\frac{\kappa}{4\pi} \oint_{\mathcal{L}} \frac{(\mathbf{s} - \mathbf{r})}{|\mathbf{s} - \mathbf{r}|^3} \times d\mathbf{r}, \quad (21)$$

where ξ is arc length and the line integral extends over the entire vortex configuration. Equation (21) expresses incompressible Euler dynamics in integral form¹⁵. Physically, it assumes that the density of the fluid is constant (zero Mach number limit) and that the vortex core is much smaller than any other length scale in the flow (a small parameter must be introduced to de-singularise the integral). Vortex reconnections are forbidden by Euler dynamics, therefore, when applying equation (21) to superfluid helium, we must supplement it with an algorithmic reconnection procedure which changes the topology of two vortex filaments when the distance between them is less than a prescribed cutoff value, as first explained by Schwarz^{23,24}. The numerical techniques which we use to compute Biot-Savart evolution are described in our previous papers^{42,43}. Here it suffices to say that the vortex filaments are discretized into a variable number of points \mathbf{s}_j ($j = 1, \dots, N$), holding their relative distance approximately between $\Delta\xi$ and $\Delta\xi/2$ where $\Delta\xi$ represents the prescribed numerical resolution. The reconnection algorithm which we use, which is triggered when the vortex separation is closer than $\Delta\xi/2$, has been already described in detail⁴⁴ and compared to other algorithms used in the liquid helium literature. It must be stressed that, unlike some of our recent work on quantum turbulence⁴⁵, the results which we present here do not use a tree-algorithm⁴⁶ to approximate and speed up the calculation of Biot-Savart integrals.

We perform our calculations in an open domain with numerical resolution $\Delta\xi = 0.0005$ cm. The initial condition of the first numerical calculation which we present consists of two vortex rings of the same polarity and radius $R = 0.0477$ cm set parallel to each other, side-by-side on the xz -plane and travelling in the y -direction, initially at distance $\Delta x = 0.002$ cm from each other. The initial number of discretization points for the two rings is $N = 1600$. The same initial condition was used by de Waele & Aarts²⁷. Figure (12) shows the time evolution. Note that the resulting vortex reconnection is locally anti-parallel ($\beta = \pi$). The initial condition of the second numerical calculation consists of the same two rings, but initially set perpendicular to each other. The time evolution is shown in figure (13). Note that the resulting reconnection is locally orthogonal ($\beta = \pi/2$).

The minimum distance between vortices, δ , for both parallel and perpendicular rings, is shown in figure (14). It is apparent that the temporal scaling is time symmetric before and after the reconnection, in agreement with equation (3) with $\alpha = 0.5$ and with the results of de Waele & Aarts²⁷. The time-symmetry of Biot-Savart reconnections contrast the time-asymmetry of GPE reconnections showed in the previous sections and of classical reconnections⁹. We tested the dependence of this result on the reconnection algorithm used⁴⁴, and found no difference in the scaling. This is perhaps not surprising as a change of the reconnection algorithm would imply a change of δ of the order of $\Delta\xi \approx 10^{-4}$ cm only, whilst we measure the evolution of δ up to distances of the order 10^{-2} cm.

The coefficient A however is not the same in all cases (although, for the approach of parallel rings, it is in fair agreement with de Waele & Aarts²⁷). A similar spread was observed by Tsubota & Adachi⁴⁷. The speed at which the vortex lines move away from each other after the reconnection is faster than the speed at which they approach each other; this effect is also visible in figures (14), and qualitatively consistent with the findings obtained with the GPE, see figure (7).

IV. CONCLUSION

Hussain & Duraisamy⁹ have shown that, in ordinary incompressible viscous fluids, the minimum separation δ between reconnecting vortex tubes behaves differently before ($\delta(t) \sim (t_0 - t)^{3/4}$) and after ($\delta(t) \sim (t - t_0)^2$) the reconnection at $t = t_0$. By solving the GPE we find a similar time asymmetry, although with different power laws: $\delta(t) \sim (t_0 - t)^{0.4}$ and $\delta(t) \sim (t - t_0)^{0.7}$ respectively, independently of the initial angle between the vortex lines. On the contrary, by solving the Biot-Savart equation, we find that the scaling is time symmetric, with $\delta(t) \sim |t_0 - t|^{1/2}$ for both $t < t_0$ and $t > t_0$.

What causes the difference? The main difference between the GPE model and the Biot-Savart model is that the former is compressible and the latter is not. Clearly the rarefaction wave which is generated at the GPE reconnection breaks the time symmetry, transforming²⁸ some of the kinetic energy of the vortices into acoustic energy which is radiated to infinity (in analogy with the viscous dissipation of kinetic energy at Navier-Stokes reconnections). The fact that GPE reconnections do not follow the power law (3) predicted by the simple dimensional argument is not surprising: at the very small scales explored by solving the GPE, other parameters besides the quantum of circulation may be relevant in determining δ , for example the coherence length.

It is also clear that the Biot-Savart model and the GPE model probe different length scales. As remarked in Section II, the GPE should converge to incompressible Euler behaviour in the limit $v/c \ll 1$ of small velocity v compared to the speed of sound c . The velocity of a vortex strand of local curvature R is approximately $v \approx \kappa/R$,

hence we expect to recover the Biot-Savart law for $R \gg \kappa/c$. However, as noticed earlier, the GPE is only a qualitative model of helium. In estimating κ/c we should not use the observed value $c = 238$ m/s, but rather the value of c which arises from the GPE itself, consistently with the vortex core size resulting from the GPE. The first step is to identify the coherence length ζ_0 . Experiments with ions and vortex rings by Rayfield and Reif suggest^{38,39} that the radius of the vortex core is $a_0 = 1.3 \times 10^{-8}$ cm. Figure 1 (right) shows that the density raises from zero to half of its value at infinity at distance $1.5\zeta_0$ (1.5 dimensionless units) from the axis of the vortex. Taking this distance as the (arbitrary but reasonable) value of the vortex core radius a_0 , we have $\zeta_0 = 0.87 \times 10^{-8}$ cm. The half-size of our computational box (30 coherence length units) thus corresponds to 26×10^{-8} cm. The second step is to find the sound speed in the GPE evolution. From $c = \sqrt{E_0/m}$ and $\zeta_0 = \hbar/\sqrt{2mE_0}$, we have $c = \hbar/(\sqrt{2}m\zeta_0) = 129$ m/s, where $m = 6.64 \times 10^{-24}$ g is the mass of one helium atom. We conclude that GPE evolution should become similar to Biot-Savart evolution for $R \gg \kappa/c \approx 8 \times 10^{-8}$ cm, that is to say for $R \gg 9\zeta_0$ (radius of curvature much greater than 9 dimensionless units). It is apparent in figures 3, 5 and 6 that the radius of curvature of the vortex line(s) near the reconnecting point, which determines $\delta(t)$, is still too small to satisfy this condition.

The Biot-Savart model assumes scales much larger than the vortex core, which is effectively neglected. So it is not possible, as a matter of principle, to use the Biot-Savart model to study behaviour at the scale of the coherence length. Neither is possible, for practical computing reasons, to solve the GPE at the large scales explored by Biot-Savart calculations such as those in section (III F).

The experimental observations of Paoletti *et al.*⁷ agree with the Biot-Savart results in terms of the time symmetry and the exponent $\alpha = 0.5$ of the power law (but it must be noticed that, for the GPE model, the average of the exponents before and after the reconnection is the same $\alpha \approx 0.5$ found in the experiment). In the experiment, the motion of the vortex lines was detected using solid hydrogen tracer particles of radius $R \approx 10^{-4}$ cm, ten thousand times larger than the coherence length in superfluid ⁴He. The rarefaction wave generated by GPE reconnections has a wavelength of about ten times the coherence length; although it is very deep initially, it quickly spreads out and vanishes as it moves away. On the scale of the tracer particles, the density of the fluid is thus constant, so it is not surprising that the Biot-Savart model is a better approximation to the observed dynamics of the vortex lines.

Finally, the spread of the values of the coefficient A which we compute and the similar spread observed in the experiment is likely to arise from differences in the initial condition, geometry of nearby vortex lines and the velocity gradients which they induce, as discussed by Paoletti *et al.*⁷.

ACKNOWLEDGMENTS

We thank the Leverhulme Trust and EPSRC for financial support.

Appendix A: Numerical method for the GPE

Without loss of generality, and for sake of simplicity, we describe in detail the numerical method applied to the one-dimensional case of equation (9) and report at the end of the section the straightforward generalization to the three-dimensional case. It is convenient to split the GPE evolution in two time steps⁴⁸:

$$\psi_t = \frac{i}{2} \nabla^2 \psi, \quad (\text{A1})$$

$$\psi_t = \frac{i}{2} (1 - |\psi|^2) \psi, \quad (\text{A2})$$

thus separating linear and non-linear operators, where the subscript t denotes the time derivative. We assume that the solution is periodic in the domain $a \leq x < b$, i.e. $\psi(a) = \psi(b)$, and seek a numerical solution in the time interval $0 \leq t \leq T$ by expanding ψ via Fourier transform as

$$\psi(x, t) = \sum_{j=-\frac{M}{2}}^{\frac{M}{2}-1} \phi_j(t) \mathcal{F}_j(x), \quad a \leq x < b, \quad 0 \leq t \leq T, \quad (\text{A3})$$

where M is the number of modes, $\phi_j(t)$ are the time-dependent Fourier coefficients, and the functions $\mathcal{F}_j(x) = \frac{1}{\sqrt{b-a}} e^{i2\pi j \frac{x-a}{b-a}}$ are orthonormal (i.e. $\int_a^b \mathcal{F}_j \overline{\mathcal{F}_k} dx = \int_a^b \mathcal{F}_j \mathcal{F}_{-k} dx = \delta_{jk}$). By computing the temporal and spatial

derivatives of ψ , substituting them in equation (A2), multiplying the latter times $\overline{\mathcal{F}}_k$, integrating between a and b , and using the orthonormality property of the functions \mathcal{F} , equation (A2) reads

$$\phi'_k(t) = \frac{i}{2}\lambda_k\phi_k(t), \quad -\frac{M}{2} \leq k < \frac{M}{2}, \quad 0 \leq t \leq T, \quad (\text{A4})$$

where $\lambda_j = -\left(\frac{2\pi j}{b-a}\right)^2$ is real and negative. The solution is, trivially,

$$\phi_k(t) = e^{t\frac{i}{2}\lambda_k}\phi_k(0). \quad (\text{A5})$$

Since both t and λ are real, $|\phi_j(t)|^2 = |\phi_j(0)|^2$ for all j . Therefore, the total mass m is preserved:

$$m(t) = \|\psi(t)\|_{L^2}^2 = \int_a^b \psi(x,t)\overline{\psi}(x,t) dx = \sum_{j=-\frac{M}{2}}^{\frac{M}{2}-1} |\phi_j(t)|^2 = \sum_{j=-\frac{M}{2}}^{\frac{M}{2}-1} |\phi_j(t_0)|^2 = \|\psi(0)\|_{L^2}^2 = m(0). \quad (\text{A6})$$

Moreover, if $\vec{\phi}$ denotes the vector of Fourier coefficients $\vec{\phi} = [\phi_{-\frac{M}{2}}, \dots, \phi_{\frac{M}{2}}]$, then

$$\|\psi(t)\|_{L^2}^2 = \|\vec{\phi}(t)\|_2^2 = \|\vec{\phi}(t_0)\|_2^2 = m(t_0) = m, \quad (\text{A7})$$

and the total mass m can be retrieved simply as the square of the norm of the complex-coefficient vector $\vec{\phi}$.

The second part of the time-splitting scheme preserves mass as well. This is easily proved by taking the conjugate of equation (A2); from $\psi_t = (i/2)(1 - |\psi|^2)\psi$ we obtain $\overline{\psi}_t = (-i/2)(1 - |\psi|^2)\overline{\psi}$, hence the derivative of $|\psi|^2$ with respect to t is

$$\frac{\partial|\psi|^2}{\partial t} = \frac{\partial\psi\overline{\psi}}{\partial t} = \psi_t\overline{\psi} + \psi\overline{\psi}_t = \frac{i}{2}(1 - |\psi|^2)\psi\overline{\psi} + \psi\left[-\frac{i}{2}(1 - |\psi|^2)\overline{\psi}\right] = 0. \quad (\text{A8})$$

The time independence of $|\psi|^2$ is crucial because it implies that the solution of equation (A2) is simply

$$\psi(x,t) = e^{t\frac{i}{2}(1 - |\psi(x,0)|^2)}\psi(x,0). \quad (\text{A9})$$

The above method can be generalised naturally to the three-dimensional case. The unknown function $\psi(x,y,z,t)$ is expanded as

$$\psi(x,y,z,t) = \sum_{j,k,l} \phi_{jkl}(t)\mathcal{F}_j(x)\mathcal{F}_k(y)\mathcal{F}_l(z), \quad (\text{A10})$$

where we use the notation $\sum_{j,k,l} = \sum_{j=-\frac{M_x}{2}}^{\frac{M_x}{2}} \sum_{k=-\frac{M_y}{2}}^{\frac{M_y}{2}} \sum_{l=-\frac{M_z}{2}}^{\frac{M_z}{2}}$.

After computing the temporal and spatial derivatives of ψ , substituting them in equation (A2), multiplying the differential equation times $\overline{\mathcal{F}}_m(x)\overline{\mathcal{F}}_n(y)\overline{\mathcal{F}}_s(z)$, integrating in space, and using the orthonormality property of the functions \mathcal{F} , the first part of the splitting now becomes

$$\phi'_{jkl}(t) = \frac{i}{2}\lambda_{jkl}\phi_{jkl}(t), \quad (\text{A11})$$

where

$$\lambda_{jkl} = -\left(\frac{2\pi j}{b_x - a_x}\right)^2 - \left(\frac{2\pi k}{b_y - a_y}\right)^2 - \left(\frac{2\pi l}{b_z - a_z}\right)^2$$

is real and negative and the mass-preserving solution is

$$\phi_{jkl}(t) = e^{t\frac{i}{2}\lambda_{jkl}} \phi_{jkl}(0).$$

As explained earlier, the second part of the splitting preserves mass too, and its solution is explicit.

In order to outline the numerical algorithm it is convenient to formulate the partial differential equation (9) as an ordinary differential equation suppressing the spatial dependence and replacing $\psi(\cdot, t)$ with $u(t)$ ⁴⁹. We obtain the initial value problem

$$u'(t) = [A + B(u(t))] u(t), \quad u(t_0) = u_0, \quad (\text{A12})$$

Using second-order Strang splitting⁵¹, the solution $u(t) = u(k\Delta t) = u_k$ can be recursively determined by the multiplication

$$u^{k+1} = e^{\frac{\Delta t}{2}B} e^{\Delta t A} e^{\frac{\Delta t}{2}B} u^k. \quad (\text{A13})$$

In our case $A = \frac{i}{2}\nabla^2$ and $B(u(t)) = \frac{i}{2}(1 - |u(t)|^2)$. As previously shown, $|u(t)|^2 = |\psi|^2$ is constant, thus both operators A and B are linear.

Since both solutions of the two parts of the splitting are explicit, the only numerical error introduced by the method is confined to the computation of the Fourier transform and its inverse. The second order error in time due to the Strang splitting can be improved to fourth order without further numerical complications⁵⁰.

In conclusion, assuming that the initial condition $\psi(x, y, z, t_0)$ is periodic in all spatial directions, the resulting algorithm is:

1. $\tilde{\psi}(x, y, z, t_0) = e^{\frac{\Delta t}{2}\frac{i}{2}(1-|\psi(t_0,x)|^2)}\psi(x, y, z, t_0)$: operator B is applied in physical space
2. $\vec{\phi}(t_0) = \text{FFT}(\tilde{\psi}(x, y, z, t_0))$: Fourier transform is applied
3. $\phi_{jkl}(t_0 + \frac{\Delta t}{2}) = e^{\Delta t\frac{i}{2}\lambda_{jkl}}\phi_{jkl}(t_0) \forall i, j, k$: operator $A = \frac{i}{2}\nabla^2$ is applied in Fourier space
4. $\tilde{\psi}(x, y, z, t_0 + \frac{\Delta t}{2}) = \text{IFFT}(\vec{\phi}(t_0 + \frac{\Delta t}{2}))$: inverse Fourier transform is applied to go back to physical space
5. $\psi(x, y, z, t_0 + \Delta t) = e^{\frac{\Delta t}{2}\frac{i}{2}(1-|\tilde{\psi}(x,y,z,t_0+\frac{\Delta t}{2})|^2)}\tilde{\psi}(x, y, z, t_0 + \frac{\Delta t}{2})$: operator $B = \frac{i}{2}(1 - |u(t)|^2)$ is applied in physical space

Clearly, step 5 is needed only to retrieve the physical solution $\psi_k(x, y, z)$ at a certain time $t = k\Delta t$, otherwise it can be avoided by merging step 5 and step 1 a single time step Δt .

The limit of this scheme is that the initial condition $\psi_0(x, y, z)$ must be periodic. If it is not, it must be made periodic by adding image vortices on a larger domain, i.e. more computational effort is required. However, certain geometries (such as two anti-parallel vortices aligned along the z -direction, moving along x and centered in $(x_0; \pm y_0)$) allow us to double the grid points only in the x -direction due to the symmetry with respect to the $y = 0$ and $z = 0$ planes. In general, if all vortices are aligned along one axis (typically z), image vortices must be introduced in both other directions. For general geometries images vortices must be introduced in all directions, causing a memory allocation eight times larger.

¹S. Kida and M. Takaoka, "Vortex reconnection", *Annu. Rev. Fluid Mech.* **26**, 169 (1994).

²P. E. Dimotakis, "Turbulent mixing", *Annu. Rev. Fluid Mech.* **37**, 329 (2005).

³A. K. M. F. Hussain, "Coherent structures—reality and myth", *Phys. Fluids* **26**, 2816 (1983).

⁴A. K. M. F. Hussain, "Coherent structures and turbulence", *J. Fluid Mech.* **173**, 303 (1986).

⁵D.R. Poole, H. Scofield, C.F. Barenghi, and D.C. Samuels, "Geometry and topology of superfluid turbulence", *J. Low Temp. Phys.* **132**, 97 (2003).

⁶R. J. Donnelly, *Quantized Vortices In Helium II*, Cambridge University Press, Cambridge, (1991).

⁷M. S. Paoletti, M. E. Fisher, and D. P. Lathrop, "Reconnection dynamics for quantized vortices", *Physica D* **239**, 1367 (2010).

⁸L. Skrebk and K.R. Sreenivasan, "Developed quantum turbulence and its decay", *Physics of Fluids* **24**, 011301 (2012).

⁹F. Hussain and K. Duraisamy, "Mechanics of viscous vortex reconnection", *Phys. Fluids* **23**, 021701 (2011).

¹⁰S. C. Crow, "Stability theory for a pair of trailing vortices", *AIAA J.* **8**, 2172 (1970).

¹¹T. Fohl and J. S. Turner, "Colliding vortex rings", *Phys. Fluids* **18**, 433 (1975).

¹²Y. Oshima and S. Asaka, "Interaction of two vortex rings along parallel axes in air", *J. Phys. Soc. Jpn.* **42**, 708 (1977).

¹³Y. Oshima and N. Izutsu, "Cross-linking of two vortex rings", *Phys. Fluids* **31**, 2401 (1988).

¹⁴W. I. Ashurst and D. I. Meiron, "Numerical study of vortex reconnection", *Phys. Rev. Lett.* **58**, 1632 (1987).

¹⁵P.G. Saffman, *Vortex Dynamics*, Cambridge University Press, Cambridge (1992).

- ¹⁶A. Pumir and R. M. Kerr, “Numerical simulation of interacting vortex tubes”, *Phys. Rev. Lett.* **58**, 1636 (1987).
- ¹⁷J. Marshall, P. Brancher, and A. Giovannini, “Interaction of unequal anti-parallel vortex tubes”, *J. Fluid Mech.* **446**, 229 (2001).
- ¹⁸P. Chatelain, D. Kivotides, and A. Leonard, “Reconnection of colliding vortex rings”, *Phys. Rev. Lett.* **90**, 054501 (2003).
- ¹⁹D. Kivotides and A. Leonard, “Computational model of vortex reconnection”, *Europhys. Lett.* **63**, 354 (2003).
- ²⁰N. K.-R. Kevlahan, “Stochastic differential equation models of vortex merging and reconnection”, *Phys. Fluids* **17**, 065107 (2005).
- ²¹B. K. Shivamoggi, “Vortex stretching and reconnection in a compressible fluid”, *Eur. Phys. J. B*, **49**, 483 (2006).
- ²²R.P. Feynman, “Application of quantum mechanics to liquid helium”, in *Progress in Low Temperature Physics*, edited by C. J. Gorter (North-Holland, Amsterdam, 1955), Vol 1.
- ²³K. W. Schwarz, “Three-dimensional vortex dynamics in superfluid ^4He : line-line and line-boundary interactions”, *Phys. Lett. B* **31** 5782 (1985).
- ²⁴K. W. Schwarz, “Three-dimensional vortex dynamics in superfluid ^4He : homogeneous superfluid turbulence”, *Phys. Lett. B* **38** 2398 (1988).
- ²⁵R. L. Ricca, “The contributions of Da Rios and Levi-Civita to asymptotic potential theory and vortex filament dynamics”, *Fluid. Dyn. Res.* **18**, 245 (1996).
- ²⁶J. Koplik and H. Levine, “Vortex reconnection in superfluid helium”, *Phys. Rev. Lett.* **71**, 1375 (1993).
- ²⁷A. T. A. M. de Waele and R. G. K. M. Aarts, “Route to vortex reconnection”, *Phys. Rev. Lett.* **72**, 482 (1994).
- ²⁸M. Leadbeater, T. Winiecki, D.C. Samuels, C.F. Barenghi and C.S. Adams, “Sound emission due to superfluid vortex reconnections”, *Phys. Rev. Letters* **86**, 1410 (2001)
- ²⁹W.F. Vinen, “Decay of superfluid turbulence at very low temperature: the radiation of sound from a Kelvin wave on a quantized vortex”, *Phys. Rev. B* **64**, 134520 (2001).
- ³⁰M. Leadbeater, D.C. Samuels, C.F. Barenghi and C.S. Adams, “Decay of superfluid turbulence via Kelvin-wave radiation”, *Phys. Rev. A* **67**, 015601 (2003).
- ³¹W.F. Vinen and J.J. Niemela, “Quantum turbulence”, *J. Low Temp. Physics* **128**, 167 (2002).
- ³²R. Tebbs, A. J. Youd, and C. F. Barenghi, “The approach to vortex reconnection”, *J. Low. Temp. Phys.* **162**, 314 (2011).
- ³³M. Kursa, K. Bajer, and T. Lipniacki, “The approach to vortex reconnection”, *Phys. Rev. B* **83**, 014515 (2011).
- ³⁴R. M. Kerr, “Vortex stretching as a mechanism for quantum kinetic energy decay”, *Phys. Rev. Lett.* **106**, 224501 (2011).
- ³⁵P.H. Roberts and N.G. Berloff, The nonlinear Schrödinger equation as a model of superfluidity, in *Quantized Vortex Dynamics and Superfluid Turbulence*, ed. by C.F. Barenghi, R.J. Donnelly and W.F. Vinen, Springer Lecture Notes in Physics (2001), page 235–257.
- ³⁶M. Sadd, G. V. Chester and L. Reatto, Structure of a vortex in superfluid ^4He , *Phys. Rev. Lett.* **79**, 2490 (1997).
- ³⁷R. J. Donnelly and C.F. Barenghi, The observed properties of liquid helium at the saturated vapor pressure, *J. Phys. Chem. Ref. Data* **27**, 1217 (1998).
- ³⁸G.W. Reyfield and F. Reif, Quantized vortex rings in superfluid helium, *Phys. Rev.* **136**, A1194 (1964).
- ³⁹C.F. Barenghi, R.J. Donnelly and W.F. Vinen, Friction on quantized vortices in helium II, *J. Low temp. Phys.* **52**, 189 (1983).
- ⁴⁰N. G. Berloff, “Padè approximations of solitary wave solutions of the Gross-Pitaevskii equation”, *J. Phys. A: Math. Gen.* **37**, 1617 (2004).
- ⁴¹A. W. Baggaley, L. K. Sherwin, C. F. Barenghi, and Y. A. Sergeev, Thermally and mechanically driven quantum turbulence in helium II, *Phys. Rev. B* **86**, 104501 (2012).
- ⁴²A.W. Baggaley and C.F. Barenghi, “Spectrum of turbulent Kelvin-waves cascade in superfluid helium”, *Phys. Rev. B* **83**, 134509 (2011).
- ⁴³A.W. Baggaley and C.F. Barenghi, “Vortex-density fluctuations in quantum turbulence”, *Phys. Rev. B* **84** R, 020504 (2011)
- ⁴⁴A.W. Baggaley, “The sensitivity of the vortex filament method to different reconnection models”, *J. Low Temp. Physics*, **168**, 18 (2012)
- ⁴⁵A.W. Baggaley, C.F. Barenghi, A. Shukurov, and Y.A. Sergeev “Coherent vortex structures in quantum turbulence”, *Europhys. Lett.* **98**, 26002 (2012).
- ⁴⁶A.W. Baggaley and C.F. Barenghi, “Tree Method for quantum vortex dynamics”, *J. Low Temp. Physics* **166**, 3 (2012)
- ⁴⁷M. Tsubota & H. Adachi, “Simulation of counterflow turbulence by vortex filament”, *J. Low Temp. Phys.* **162** 367 (2011).
- ⁴⁸W. Bao & D. Jaksch, & P. Markowich, “Numerical solution of the Gross–Pitaevskii equation for Bose–Einstein condensation”, *J. Comp. Phys.* **187**, 318 (2003)
- ⁴⁹M. Thalhammer and M. Caliari and Ch. Neuhauser, ‘High-order time-splitting Hermite and Fourier spectral methods for the Gross–Pitaevskii equation”, *J. Comp. Phys.* **228**, 822 (2009)
- ⁵⁰H. Yoshida, “Construction of higher order symplectic integrators”, *Phys. Lett. A* **150**, 262 (1990).
- ⁵¹G. Strang, “On the construction and comparison of difference schemes”, *SIAM J. Numer. Anal.* **5**, 506 (1968).

angle β	A_{before}	α_{before}	A_{after}	α_{after}
$\frac{8}{8}\pi = \pi$	1.36	0.30	1.88	0.66
$\frac{7}{8}\pi = \frac{7}{8}\pi$	1.23	0.39	2.71	0.63
$\frac{6}{8}\pi = \frac{3}{4}\pi$	1.44	0.41	1.69	0.68
$\frac{5}{8}\pi = \frac{5}{8}\pi$	1.35	0.44	1.30	0.69
$\frac{4}{8}\pi = \frac{\pi}{2}$	1.41	0.36	1.01	0.67
$\frac{3}{8}\pi = \frac{3}{8}\pi$	0.94	0.42	0.66	0.73
average	1.29	0.39	1.54	0.68

TABLE I. Coefficients of the fit $\delta(t) = A|t - t_0|^\alpha$ of the minimum distance between vortices before and after the reconnection at different initial angles β .

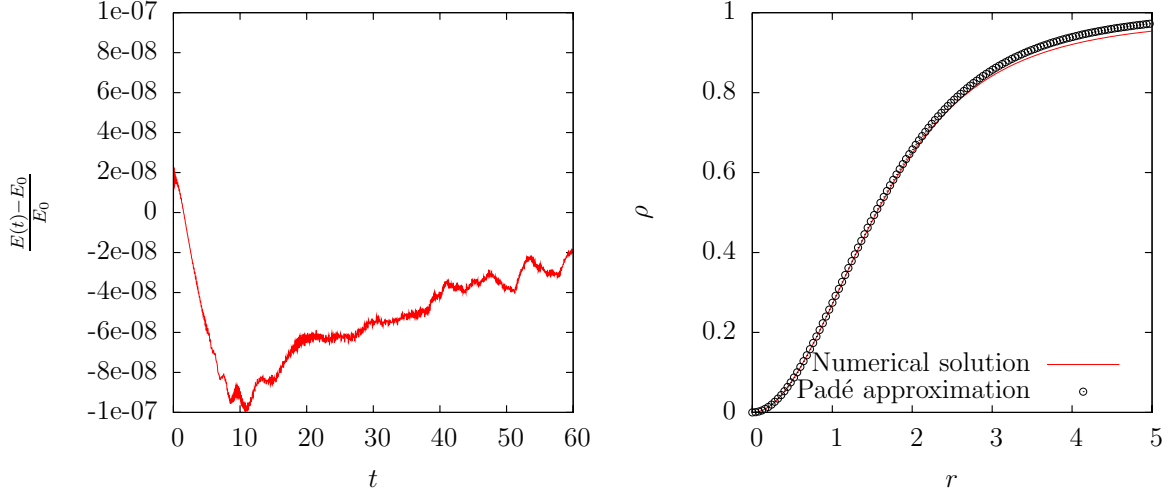


FIG. 1. Left: Relative change of the dimensionless Hamiltonian energy $E(t)$ as a function of dimensionless time t with respect to the initial energy $E_0 = E(0)$ during antiparallel reconnection. Right: Dimensionless density ρ as a function of the dimensionless radial coordinate r computed numerically (solid line, obtained by setting $r_\infty = 20$ and using 500 grid points) and with the Padé approximation (empty circles).

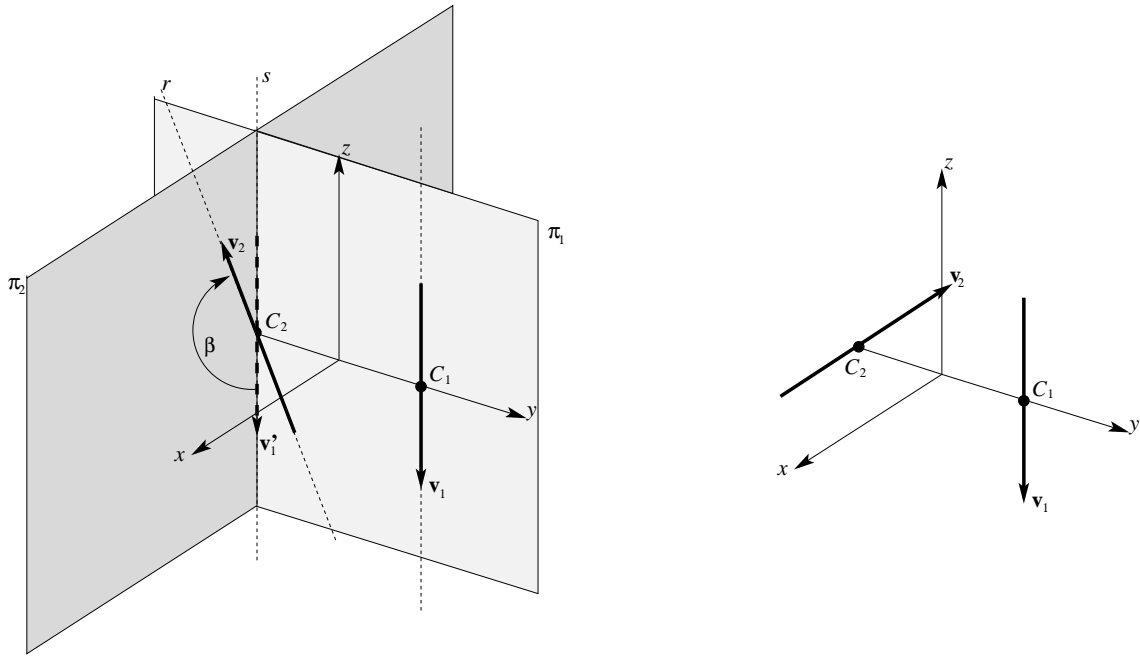


FIG. 2. Initial condition. Left: $\beta = 3\pi/4$. Right: $\beta = -\pi/2$.

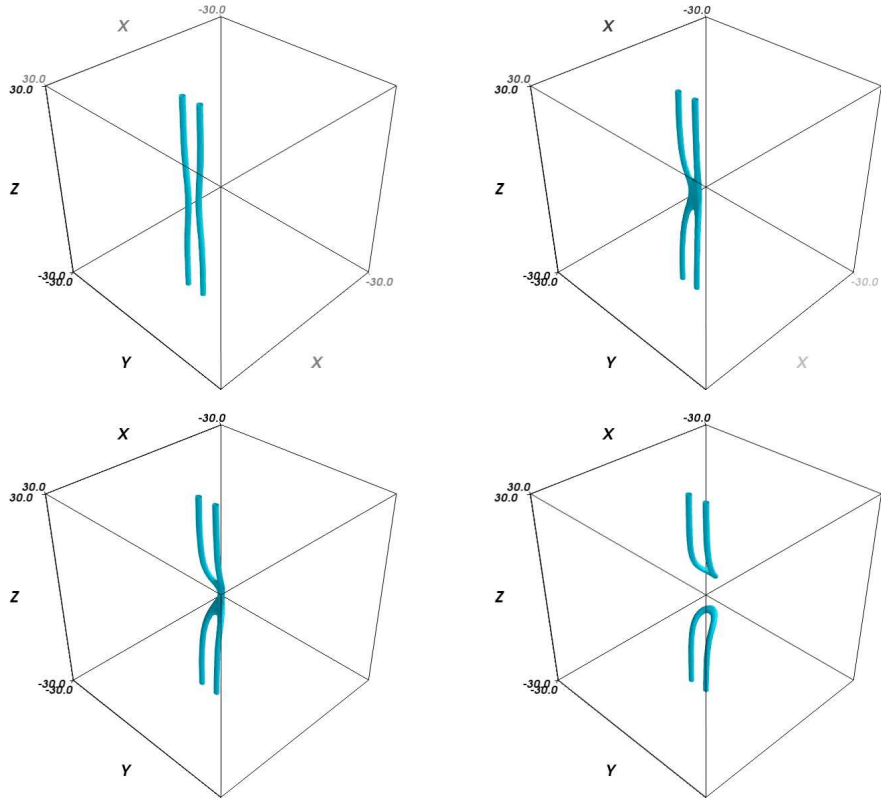


FIG. 3. Snapshots of the evolution of two anti-parallel vortices (angle between vortices $\beta = \pi$), initially slightly perturbed to enhance the Crow instability, at $t = 0$ (top left), $t = 20$ (top right), $t = 30$ (bottom left), $t = 40$ (bottom right). Isosurfaces of $\rho = 0.2$ are plotted to visualise the vortex cores.

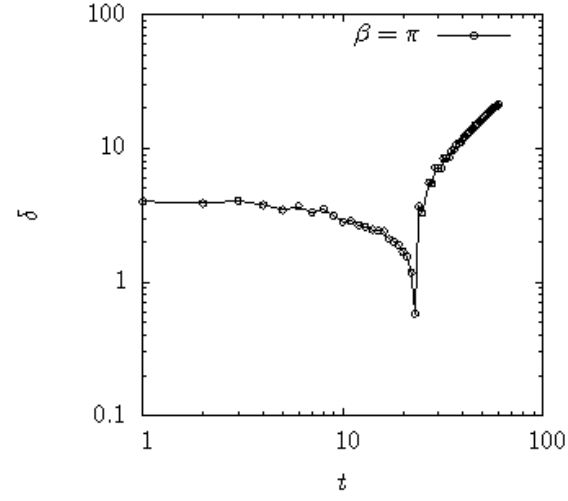


FIG. 4. Minimum distance δ between reconnecting vortices as a function of time t for the pair of reconnecting anti-parallel vortices ($\beta = \pi$) shown in figure (3).

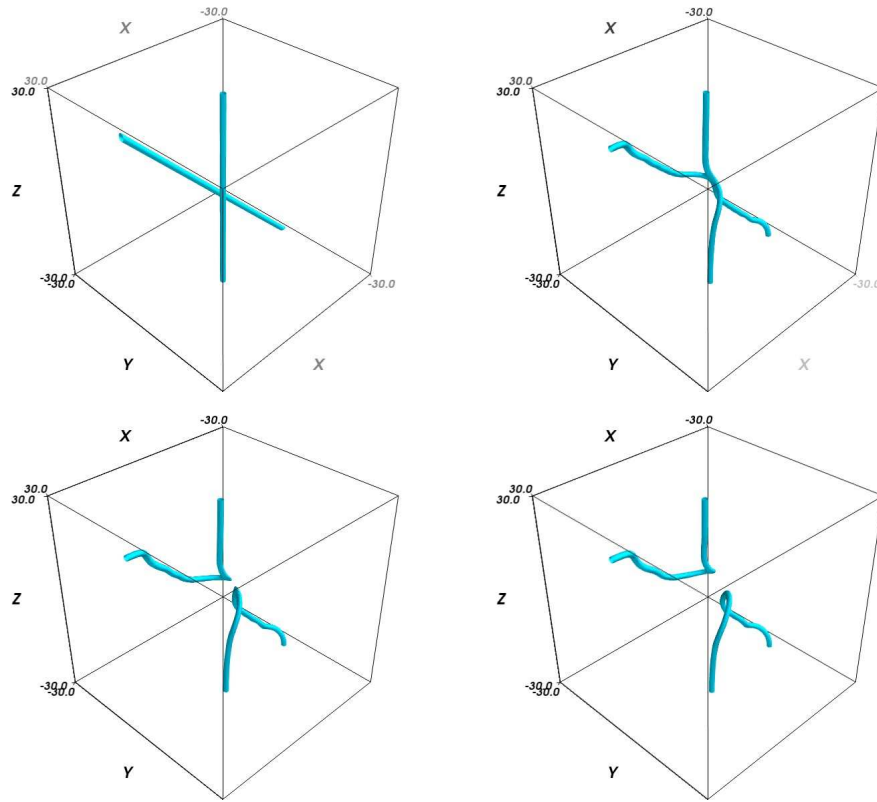


FIG. 5. Snapshots of the evolution of two initially straight vortices forming an angle $\beta = 3\pi/4$ at $t = 0$ (top left), $t = 15$ (top right), $t = 20$ (bottom left), $t = 25$ (bottom right). Isosurfaces of $\rho = 0.2$ are plotted to visualise the vortex cores.

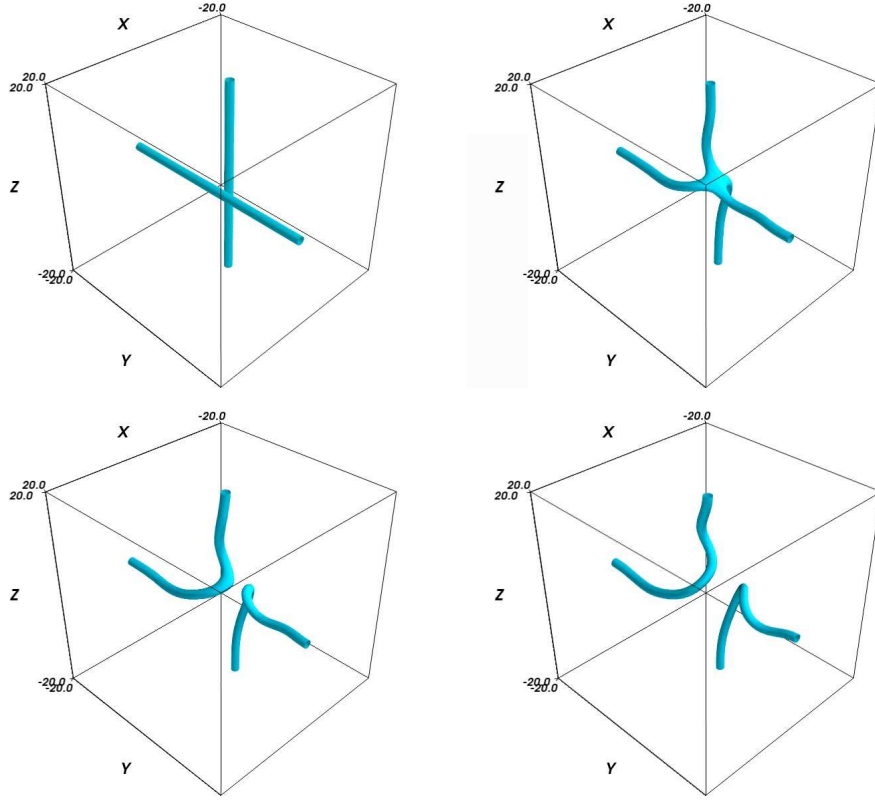


FIG. 6. Snapshots of the evolution of two perpendicular vortices (angle between vortices $\beta = \pi/2$) at $t = 0$ (top left), $t = 20$ (top right), $t = 30$ (bottom left), $t = 40$ (bottom right). Isosurfaces of $\rho = 0.2$ are plotted to visualise the vortex cores.

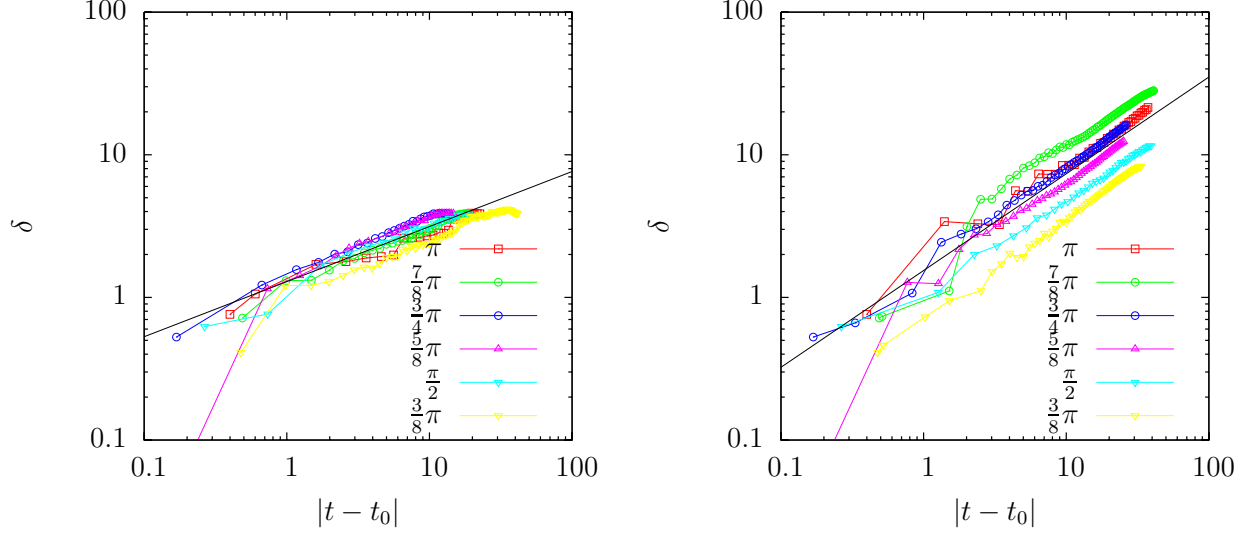


FIG. 7. Distance between vortices as a function of $|t - t_0|$ before (top) and after (bottom) the reconnection for different values of the angle β between initial vortex lines ($\beta = \pi$ refers to anti-parallel vortices, and $\beta = \pi/2$ to orthogonal vortices). The computed values are joined by lines to guide the eye. The black solid lines are fits of the form $\delta(t) = A|t - t_0|^\alpha$; the fitting coefficients A and α are reported in table I.

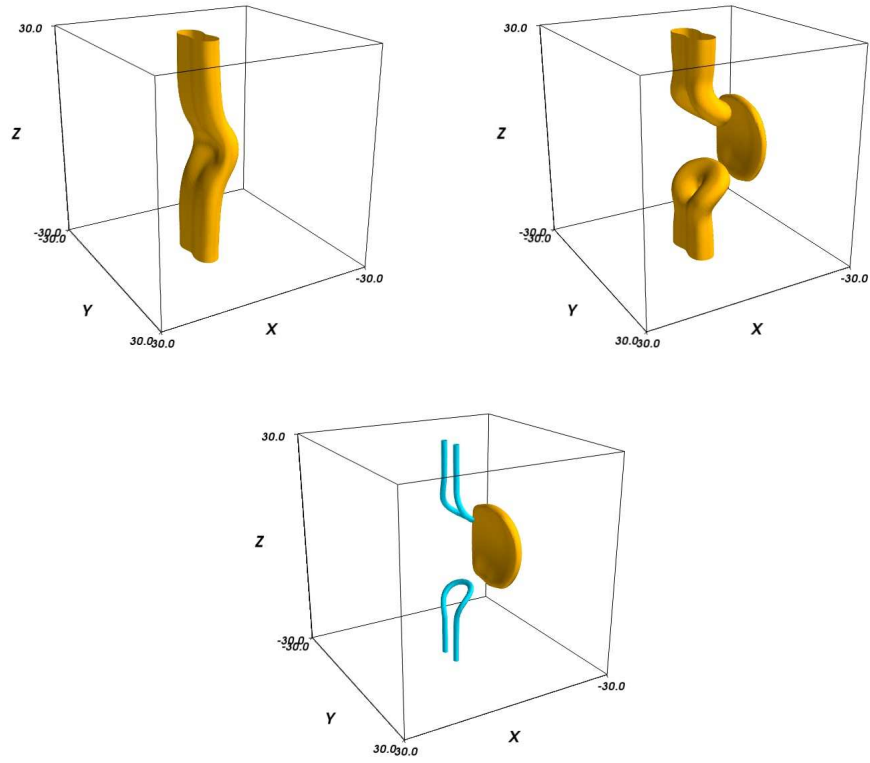


FIG. 8. Isosurfaces at $\rho = 0.94$ before (left, $t = 37$) and after (right and bottom, $t = 54$) reconnection for two anti-parallel vortices (angle between vortices $\beta = \pi$). Note the mushroom-shaped rarefaction wave which moves away.

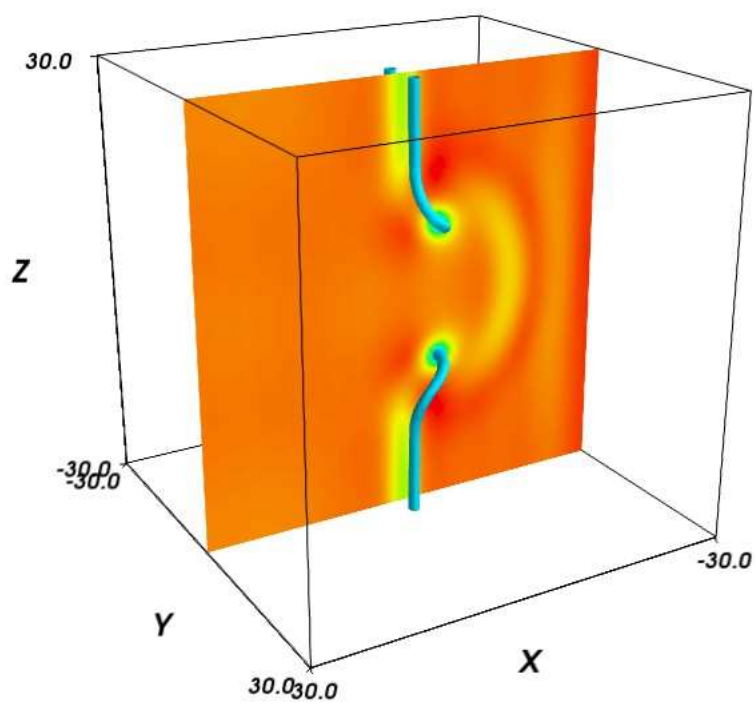


FIG. 9. Isosurfaces at ρ and $t = 54$ as in figure (8) (bottom, anti-parallel vortices) to visualise the vortex core with superimposed the profile of ρ on the $y = 0$ plane. Note the rarefaction wave.

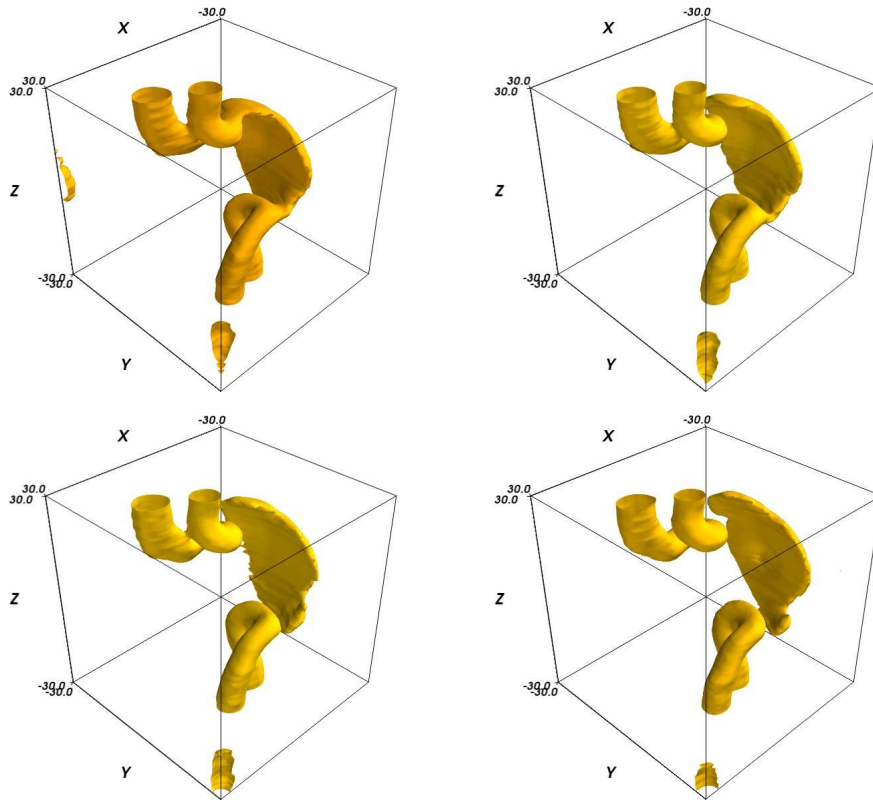


FIG. 10. Snapshots of the evolution of the mushroom-shaped rarefaction wave ejected after reconnection, $\beta = 7\pi/8$, at $t = 53$ (top left), $t = 55$ (top right), $t = 57$ (bottom left), $t = 59$ (bottom right); isosurfaces of $\rho = 0.94$ are plotted to visualize the vortex cores and the wave as in figure (8).

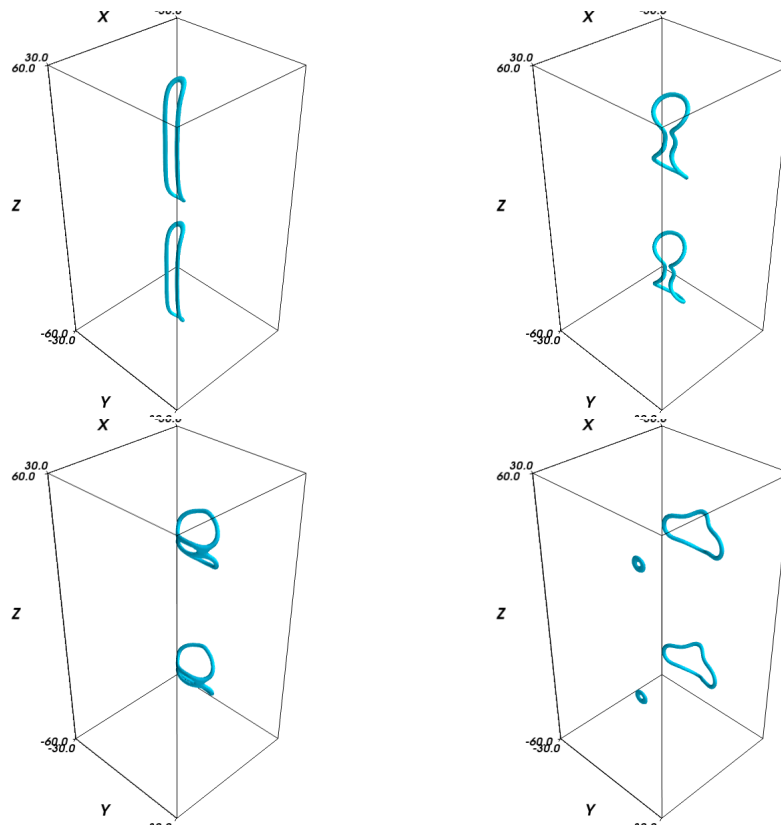


FIG. 11. Snapshots of the evolution of two antiparallel vortices (angle $\beta = \pi$) initially slightly perturbed to enhance the Crow instability, at $t = 40$ (top left), $t = 80$ (top right), $t = 120$ (bottom left) and $t = 160$ (bottom right). Isosurface of $\rho = 0.2$ are plotted to visualize the vortex cores. The initial condition is the same as in figure 3 but the computational box was extended to $-60 \leq z \leq 60$ to visualize the formation of vortex rings.

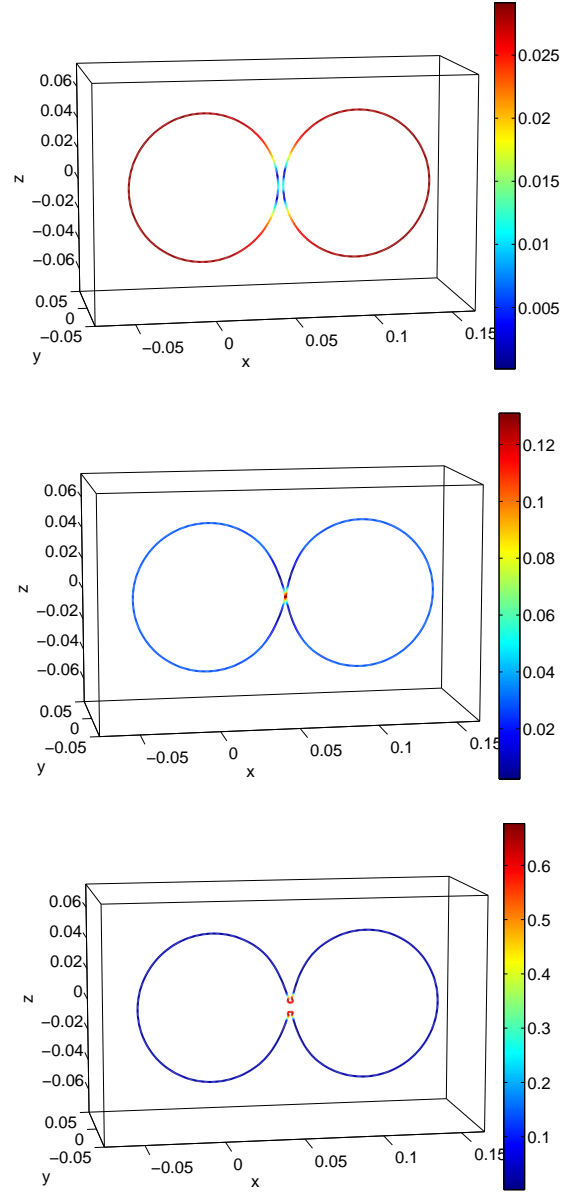


FIG. 12. Reconnection of two vortex rings initially set parallel to each other (as in the work of de Waele & Aarts²⁷), computed with the Biot-Savart law: Top: at time $t = 0$; middle: $t_0 - t = 0.001$ s; bottom: $t - t_0 = 0.005$ s. The vortex lines are colour-coded to indicate the magnitude of the velocity (in cm/s, see legend on each figure). The box is for visualization only.

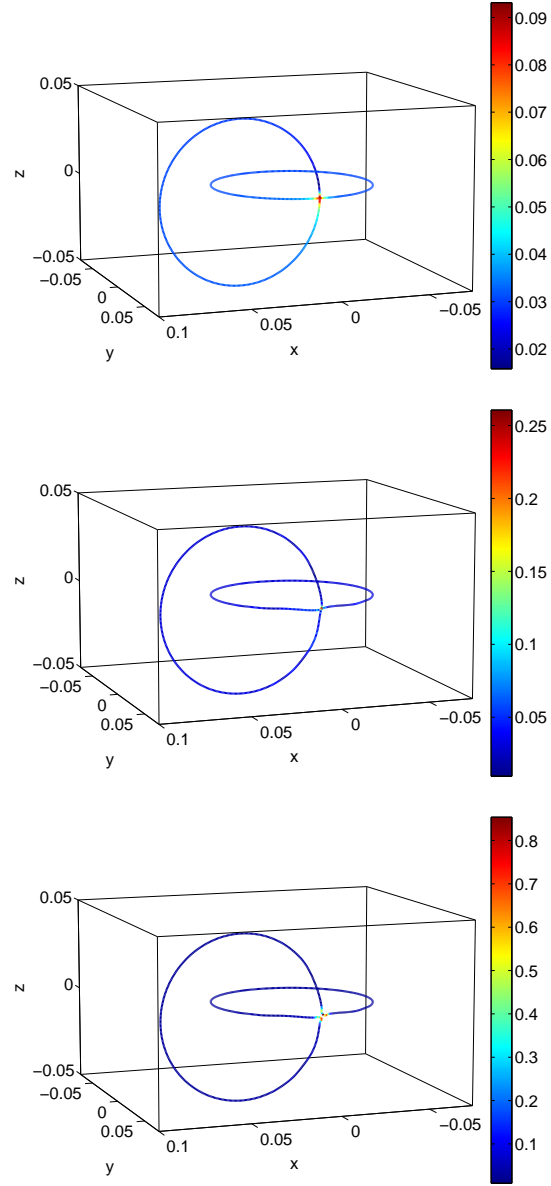


FIG. 13. Reconnection of two vortex rings initially set perpendicular to each other, computed with the Biot-Savart law: Top: at time $t = 0$; middle: $t_0 - t = 0.001$ s; bottom: $t - t_0 = 0.005$ s. The vortex lines are colour-coded to indicate the magnitude of the velocity (in cm/s, see legend on each figure). The box is for visualization only.

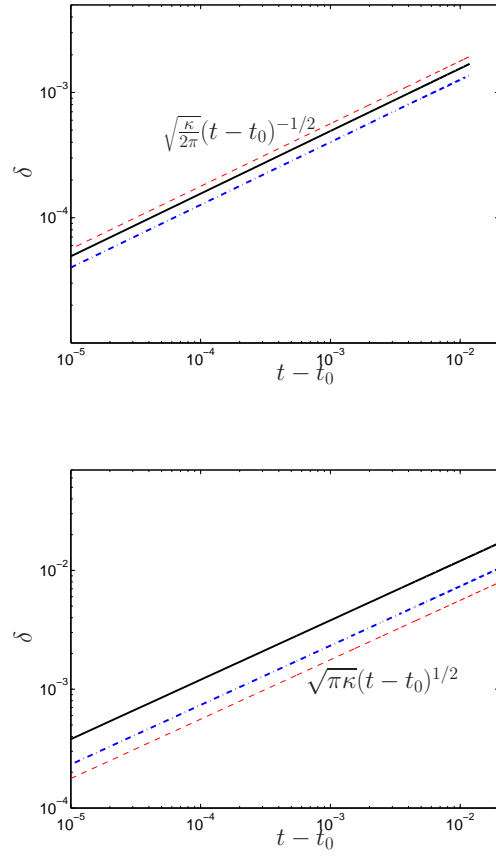


FIG. 14. Minimum distance between the filaments $\delta(t)$ (cm) vs $(t_0 - t)$ (s) before the reconnection (top) and vs $(t - t_0)$ after the reconnection (bottom), corresponding to the Biot-Savart evolution of two parallel vortex rings shown in figure (11) (solid black line) and of two perpendicular vortex rings shown in figure (12) (dot-dashed blue line). t_0 is the time at which the reconnection takes place. The dashed red line expresses $\delta(t) = \sqrt{\kappa(t_0 - t)/(2\pi)}$ found by de Waele & Aarts²⁷ (top) and $\delta(t) = \sqrt{\pi\kappa(t - t_0)}$ (bottom) as a guide to the eye.